

DropletMask: Digitizing micrometer droplet impacts

Chuanning Zhao¹ | Youngjoon Suh¹ | Yoonjin Won^{1,2,*}

¹ Mechanical and Aerospace Engineering Department, University of California, Irvine, Irvine, USA

² Electrical Engineering and Computer Science Department, University of California, Irvine, Irvine, USA

* Corresponding Author

Yoonjin Won, Samueli School of Engineering, University of California, Irvine, CA 92697.

Email: won@uci.edu

Abstract

Machine learning-assisted computer vision represents a state-of-the-art technique for extracting meaningful features from visual data autonomously. This approach facilitates the quantitative analysis of images, enabling object detection and tracking. In this study, we utilize advanced computer vision to precisely identify droplet motions and quantify their impact forces with spatiotemporal resolution at the picoliter or millisecond scale. Droplets, captured by a high-speed camera, are denoised through neuromorphic image processing. These processed images are employed to train convolutional neural networks, allowing the creation of segmented masks and bounding boxes around moving droplets. The trained networks further digitize time-varying multi-dimensional droplet features, such as droplet diameters, spreading and sliding motions, and corresponding impact forces. Our innovative method offers accurate measurement of small impact forces with a resolution of approximately 10 pico-newtons for droplets in micrometer range across various configurations with the time resolution at hundreds of microseconds.

Keywords

AI for science, machine vision, impacting droplets, digital droplets

1. Introduction

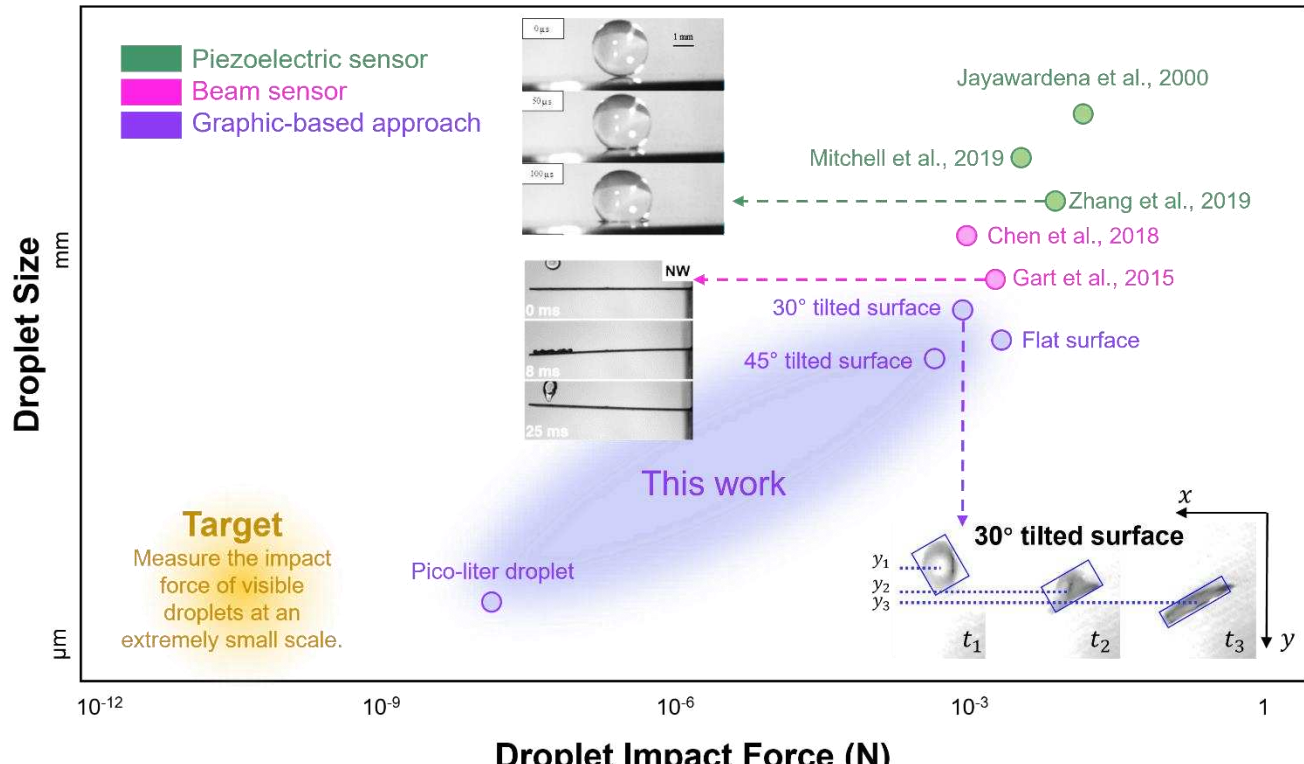


FIGURE 1 Regime map illustrates different approaches for measuring droplet impact forces. Both piezoelectric and beam sensors can measure impact forces down to 10^{-3} N. In contrast, the vision-based approach proposed in this study can measure extremely small droplets with the forces of 10^{-9} to 10^{-7} N by taking advantage of the spatiotemporal resolution of a high-speed camera.

Liquid-droplet impact behavior on flat or tilted surfaces is a fundamental phenomenon in many engineering scenarios involving mechanical components, such as solid material erosion¹, turbine blade surface damage², soil loss³, and triboelectric nanogenerators⁴. The droplet impact behavior encompasses the dynamic processes of droplet spreading, rebounding, contact angle beating⁵, droplet vibration, and droplet contact line motions⁶. Recent studies for droplet impact behaviors yield visually interpretable data on these phenomena, laying the groundwork for qualitative assessments of solid-fluid interactions during the droplet approaching and impacting processes⁷. Specifically, when it comes to the use of droplets in energy harvesting using triboelectric nanogenerator applications, such data are crucial for exploring charge transfer mechanisms and their relationships with droplet impact dynamics. However, there remains a gap in quantifiable analyses that link droplet impact behaviors with the resultant electrical signals generated from triboelectric nanogenerators, indicating an area ripe for further investigation. Understanding droplet impact behavior, as well as the magnitudes and temporal distributions of droplet impact forces, is crucial for designing and maintaining systems and components in the aforementioned scenarios.

Bridging this gap requires an accurate and automatically analyzing method to track the magnitude and temporal information of droplet locations, dimensions, and the impact forces exerted by droplets on the substrate materials. Previous researchers have employed several methods including piezoelectric sensors, beam sensors, and others to gain a complete view of the droplet impact mechanism. Researchers commonly assumed water droplets to be incompressible and used the model $F = \rho U^2 A$ to express the transient droplet impact force, where ρ is the water density, U is the droplet impact velocity just before impact, and A is the transient droplet area of contact⁸. However, this approach fails to address the compressional wave that exists in the droplet impact process. The utilization of piezoelectric sensors helps address this problem. Piezoelectric sensors are capable of directly capturing the real droplet movements on surfaces and measuring the temporal profile of droplet impact forces. Consequently, researchers extensively equip piezoelectric sensors in experiments to study the force, pressure, strain, and acceleration during the droplet impact process. For instance, a study accurately measures the times and magnitudes of droplet impact forces with 3.31, 3.83, and 4.51 mm in diameter⁹ using a piezoelectric sensor. Piezoelectric sensors are broadly used to extract the droplet impact force for low impact velocity droplets¹⁰⁻¹³, various density droplets¹², and droplet impacting processes under sub-atmospheric ambient pressure¹⁴. However, to study the dynamics of droplet impacts with high impact velocities, researchers need to combine high-speed photography techniques with piezoelectric sensors or solely rely on the theoretical analysis of the expansion fan and shock wave during high-velocity

droplet impacts¹⁵. Some studies have used numerical tools to investigate the fluid dynamics of high-impact-velocity droplets on rigid substrates^{15,16}, providing an alternative approach to exploring these extreme impact conditions instead of relying solely on piezoelectric sensor. Resolution limitations and thermal operating requirements are other drawbacks of piezoelectric sensors. The minimum achievable resolution of piezoelectric sensors is around 0.1 mg⁸, where the sensors have high temperature sensitivity. These constraints further limit the application of piezoelectric sensors in certain scenarios.

To expand the application of force sensors in various scenarios, cantilever beams present a viable option. They find widespread use in contexts including structural design sensitivity analysis¹⁷, material damping¹⁸, vibration characterization¹⁹, joining phenomena analysis²⁰, and measuring mechanical properties^{21,22}. Notably, beam sensors demonstrate promising capabilities in measuring detailed information about droplet impact on elastic substrates. On these substrates, droplet impact motions can be amplified by visually distinguishable beam deformation amplitudes and vibration frequencies at the beam tips. Common practices here include binding the piezoelectric structure to one (or both) ends of the beam²³ and assembling the beam material with polyvinylidene fluoride (PVDF)^{24,25}. Through these practices, displacements and frequencies at the beam tips are directly measured through optical methods. Researchers can then estimate the droplet impact force using the beam equations^{26,27}. However, to generate a measurable optical displacement on common elastic materials, the water droplet size is limited to several millimeters, corresponding to a droplet impact force of around several millinewtons, as illustrated in **Figure 1**. This indicates that the applications of beam sensors are also constrained by the measurement limitation.

Conventional force sensors, such as piezoelectric and beam sensors, as mentioned above, have limitations in measuring droplet impact forces. Some popular computer vision models qualify to address this concern by analyzing transient graphical data extracted from the droplet impacting process. Previous computer vision models, including edge detection and thresholding methods²⁸⁻³⁰, rely on the employment of one or multiple thresholds. In these methods, the edge locations correspond to the pixel brightness gradients, and the object and background are distinguished by clusters of varying brightness intensities, lacking the capability to process noisy data. Computer vision models like region growing³¹ and spatial clustering³² are also potential candidates for object detection. However, most of them require human intervention or additional image processing to adjust for image background differences and extract droplet impact information using a consistent standard.

With recent advances in AI-based machine learning technology, a tremendous amount of readily established artificial neural networks³³ are available and suitable for enhancing data inference. This includes tasks such as identifying and tracking moving objects from visual data. For example, a high-quality object instance segmentation framework called Mask R-CNN³⁴, which is an extension of vision-based technologies focusing on Fast R-CNN and Fully Convolutional Network (FCN). Instead of detecting objects purely based on the color intensity and distribution of images, these deep learning-enabled computer vision techniques approach the final object segmentation by learning features from multiple convolutional layers, allowing the continuous capture of these features through a sequence of images.

In pursuit of quantifying the impact force of droplets in picolitres or even smaller volumes, this work proposes a novel framework that extracts transient impact information from droplets with minimal weights. The framework begins by using experimental visual data as the optical input for the denoising module. The purpose of this module is to extract all droplet motions that can be represented by brightness variation from traditional camera videos and then convert these motions to dynamic vision sensor (DVS) videos³⁵⁻³⁷. This process helps eliminate the original video background, including the impacting substrate, noise points, and unevenly distributed LED background light. Additionally, the slomo option in this module aids in augmenting the optical input data with the existence of droplet movements. After the denoising module, we then employ a deep learning-based computer vision model to track moving objects (i.e., droplets) across frames via a customized Mask R-CNN³⁸⁻⁴⁰. The proposed framework in this work can be further extended to investigate various droplets under different conditions (e.g., droplets on surface inclination angles⁴¹, or electrically charged droplets) as long as visual data are available.

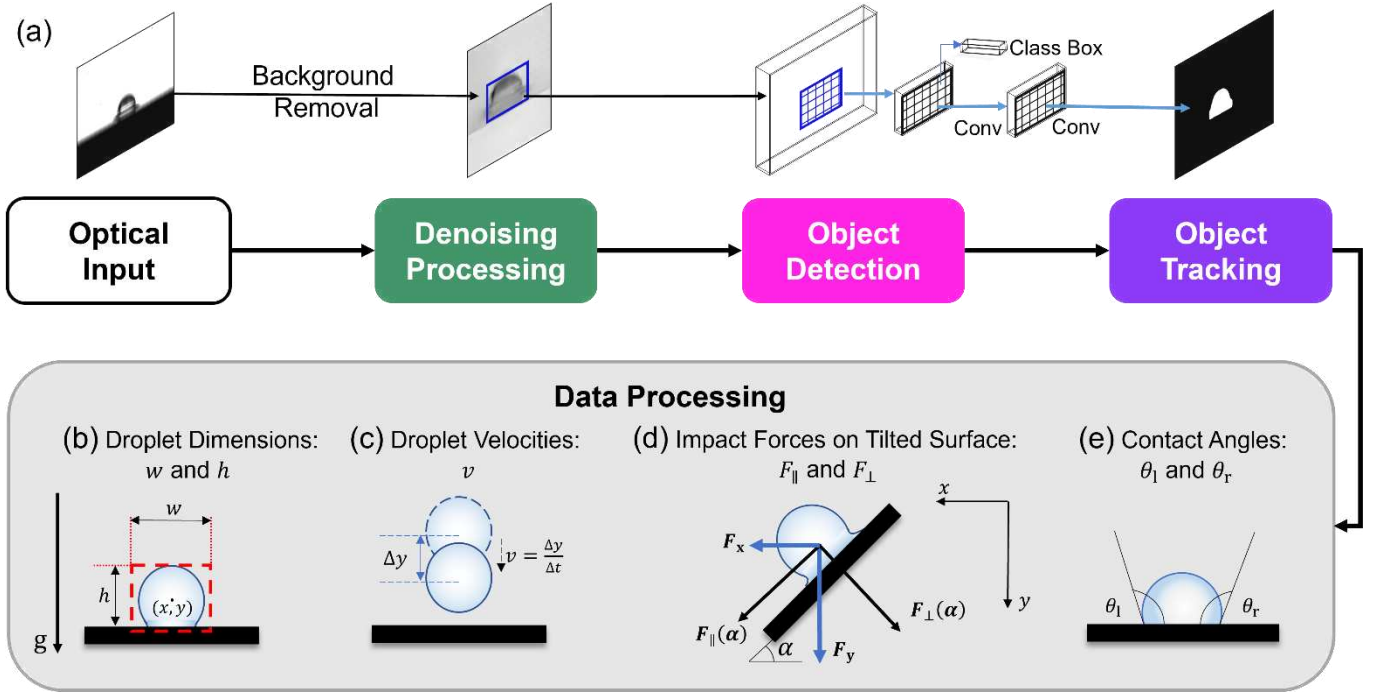


FIGURE 2 Vision-based framework for digitizing droplet impacts. (a) The proposed framework consists of optical input, denoising, object detection, object tracking, and data processing modules to obtain physically meaningful droplet features, such as: (b) droplet dimensions, (c) droplet velocities, (d) impact forces on tilted surface, and (e) contact angles.

The proposed framework consists of **denoising** processing, object detection, and object tracking where each module is assisted by AI technologies, followed by a data processing module. The **denoising** process utilizes neuromorphic processing techniques, including v2e³⁵ and the event-based image reconstruction tool e2vid^{36,37}. Notably, the **denoising** process not only aids in noise reduction but also in visual data augmentation, effectively doubling the number of images used in the impact analysis. Detailed explanations of **denoising** processes are provided in **Section 5.2** and **Supporting Information**. The object detection module incorporates a custom-trained instance segmentation model that assigns unique identifiers (IDs) to droplet masks³⁸. This module processes the **denoised** and augmented images and delivers outputs such as the droplet sizes, centroids, bounding boxes, and segmented masks. Following this, the object tracking module takes over, utilizing the IDs of detected objects associated with temporal and spatial details of each droplet to extract the statistics of the impacting droplets. This tracking process is supported by TrackPy, a dedicated toolkit^{39,40}, with comprehensive details provided in **Sections 5.3** and **5.4**. Therefore, our framework allows us to extract physically meaningful features that include instantaneous droplet centroids (x, y) , droplet dimensions (height h and width w), velocities (u and v), impact force F , and dynamic contact angles θ , where $t = 0$ sec represents the instant of droplet impact, as illustrated in **Figures 2b to 2e**. Specifically, the droplet demographics, such as droplet centroids x, y , height h , and width w , are collected based on bounding boxes from the object detection module. Here, the height and width of bounding boxes are utilized to represent the droplet dimensions h and w on both the flat and tilted surfaces, as illustrated in **Figure 2c** and the bottom-right illustration in **Figure 1**. The droplet centroids at the onset of impact are taken as the origin of the coordinates $(0,0)$.

2. Theoretical background

Once scientific features are extracted from the framework, they can be used to compute physical quantities of interest, such as velocity, acceleration, and forces. First, the changes in droplet centroid locations in the x - and y -directions are used to calculate instantaneous velocities and accelerations based on:

$$u = \frac{dx}{dt} \quad (1)$$

$$v = \frac{dy}{dt} \quad (2)$$

where the time step (Δt) is usually < 1 ms. The droplet accelerations a_x and a_y can be derived from the transient droplet impact velocities u and v , separately.

$$a_x = \frac{du}{dt} \quad (3)$$

$$a_y = \frac{dv}{dt} \quad (4)$$

As shown in the illustration from **Figure 2d**, we redefine the droplet accelerations $a_{\perp}(\alpha)$ in the perpendicular-surface direction using a_x and a_y for a surface with inclination angle α as:

$$a_{\perp}(\alpha) = -a_x \cdot \sin \alpha + a_y \cdot \cos \alpha \quad (5)$$

Here, we assume the droplet as a sphere with radius R_i which is the droplet radius at the onset of impact ($t = 0$). Then, the droplet mass m can be written as:

$$m = \rho \frac{4}{3} \pi R_i^3 \quad (6)$$

Considering all the forces (supporting force F_N , friction force F_{μ} , and gravity mg) acting on a droplet from a tilted surface, along with Newton's second law, in the perpendicular-surface direction, we obtain:

$$F_N - mg \cdot \cos \alpha = m \cdot a_{\perp}(\alpha) \quad (7)$$

where g is the gravitational acceleration. According to Newton's third law, in the perpendicular-surface direction, the combined force that a droplet experiences from the surface equals the perpendicular-surface force that a droplet exerts on the surface. Therefore, we have:

$$F_{\perp}(\alpha) = F_N = m \cdot a_{\perp}(\alpha) + mg \cdot \cos \alpha \quad (8)$$

Then, $F_{\perp}(\alpha)$ is the graphically measured droplet impact force on a surface with an inclination angle of α . **Here, the initial droplet radius R_i is used to calculate the droplet volume by assuming the droplet maintains a spherical shape right before impact.**

$$F_{\perp}(\alpha) = \rho \frac{4}{3} \pi R_i^3 \frac{du}{dt} \cdot \sin \alpha + \rho \frac{4}{3} \pi R_i^3 \frac{dv}{dt} \cdot \cos \alpha + mg \cdot \cos \alpha \quad (9)$$

On flat surfaces, with the inclination angle α of the impact surface equals to zero (i.e., $\sin 0^\circ = 0, \cos 0^\circ = 1$), Eq. (9) is rearranged as:

$$F_{\perp}(0) = \rho \frac{4}{3} \pi R_i^3 \frac{dv}{dt} + mg \quad (10)$$

We separately calculate the impact forces using a model called the *self-similarity model*^{42,43}, which proposes that the wall surface is compressible at the early stage of droplet impact, causing surface erosion and deformation to occur due to the high impact pressure along the droplet-solid contact surface. All fluid motions inside the droplet are assumed to be irrotational and axisymmetric in derivation, which might not be ideal for tilted surfaces. By assuming the droplet to be an ellipsoid, the instantaneous effective droplet diameter D_e is defined as:

$$D_e = \sqrt[3]{h \cdot w^2} \quad (11)$$

The total droplet impact force⁴² on the flat substrate is calculated starting from the Navier-Stokes equation using similarity nature to simplify the expression of pressure field during the droplet impact. By integrating the pressure between the droplet-solid contact surface as boundary conditions, the impact force $F_{\text{model}}(0)$ on a flat surface can be simplified as:

$$F_{\text{model}}(0) = 6\sqrt{3} \rho v_0^{5/2} (D_e/2)^{3/2} \sqrt{t} \quad (12)$$

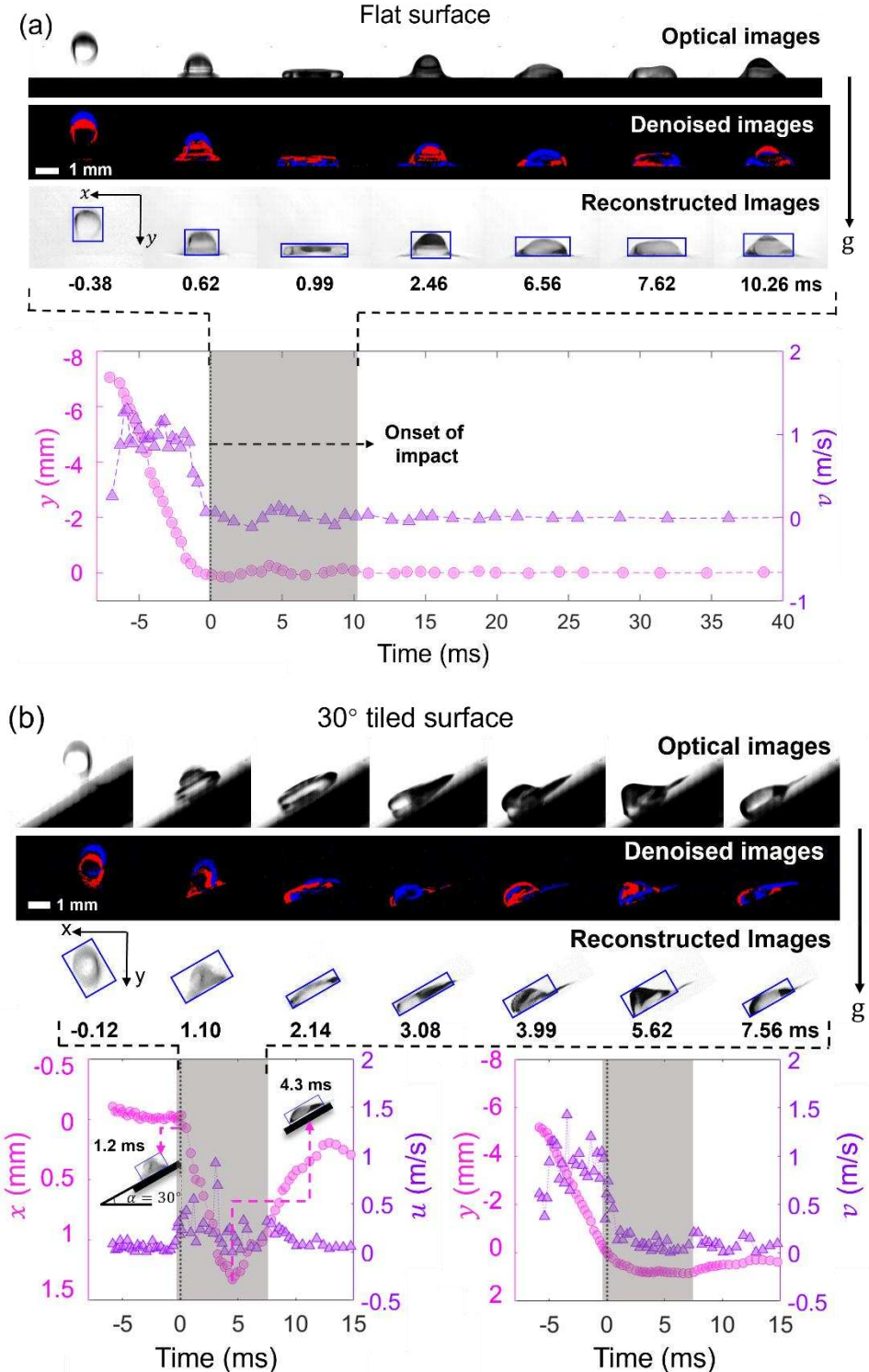
where v_0 is the average droplet velocity within 2 ms before the onset of impact. As for the droplet impact surface with an inclination angle α , we express the forces perpendicular to the surface as:

$$F_{\text{model},\perp}(\alpha) = 6\sqrt{3} \rho v_0^{5/2} (D_e/2)^{3/2} \sqrt{t} \cdot \cos \alpha \quad (13)$$

Furthermore, we quantify dynamic contact angles θ_l and θ_r by determining the intersection angles between the impacting substrate and the slope of the liquid-air interface (i.e., droplet profile) at the droplet contact points, as shown in **Figure 2e**. Additionally, we explore the frequency of dynamic contact angles by applying a non-uniform fast Fourier transform (nFFT) algorithm to the time sequences of both θ_l and θ_r .

3. Results and Discussion

3.1 Droplet impact behaviors



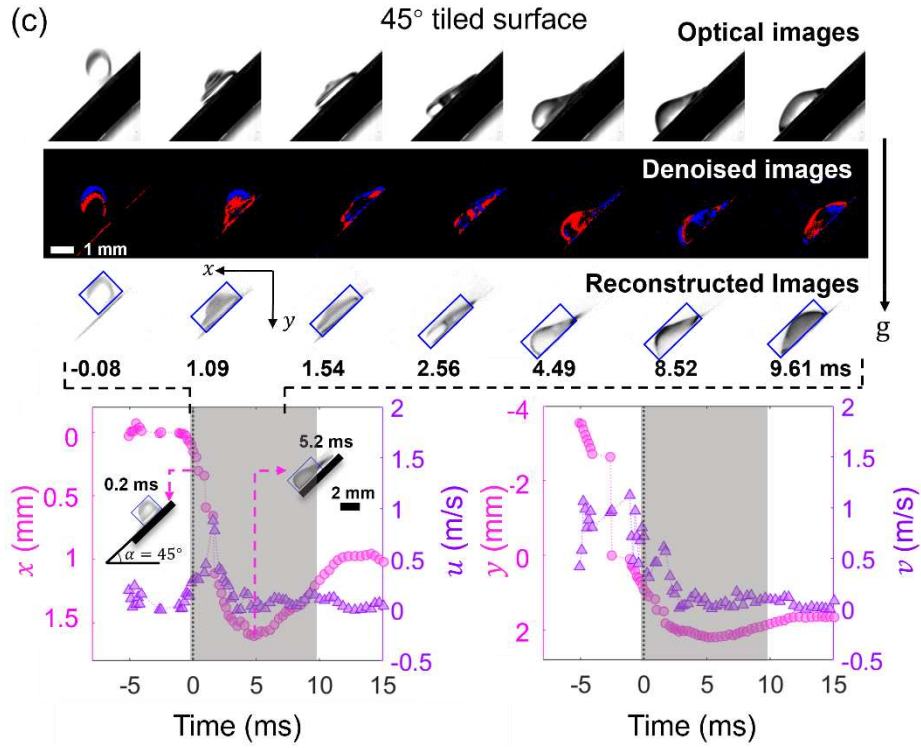


FIGURE 3 **Droplet centroid** locations and velocities on various surfaces. (a) Time-series droplet captures from a high-speed camera, neuromorphic-assisted denoising process, and reconstructed frames with object detection bounding boxes, along with y (pink circles) and v (purple triangles) on the flat bare copper surface, (b) **droplet captures** and x or y (pink circles), u or v (purple triangles) on 30° **tilted bare copper surfaces**, and (c) **droplet captures** and x or y (pink circles), u or v (purple triangles) on 45° **tilted bare copper surfaces**. Here, droplet centroids x and y are defined as the relative distance in x - and y -direction between droplet's instant location and the droplet-surface first contact at (0,0). The black dashed lines refer to the onset of droplet impact.

We focus on the analysis of droplet spreading and recoiling dynamics. It presents a series of optical, denoised, and reconstructed images that concurrently document the behavior of droplets impacting both flat and tilted surfaces within a 10-millisecond timeframe, as depicted in **Figures 3a-3c**. It should be noted that all centroid information discussed in this and subsequent sections is derived from the 2D centroid of the blue bounding box, as shown in the reconstructed images in **Figures 3a-3c**, which capture droplets from a side view. We have chosen to use the 2D centroid (x, y) as a proxy for the 3D centroid of the droplets. Here, the denoising process selectively preserves the dynamically moving objects in the optical images, thereby ensuring that the reconstructed images retain only the motion of the droplets of interest and successfully remove unnecessary background in optical images. In addition to the visual documentation, this study provides detailed temporal variations of position and velocity parameters (x, y, u , and v) associated with the droplet impact images. Before impact, the average velocities in the y -direction (v) are observed to be approximately 0.8 – 0.9 m/s. Notably, the magnitude of variation in terms of x , which physically represents the relative sliding distance from the initial impact point (where $x = 0$), is found to be larger on the 45° tilted surface (approximately 1.5 mm) compared to the 30° tilted surface (approximately 1.3 mm), as illustrated in **Figures 3b** and **3c**. Here, a positive x value indicates the droplet sliding towards the left. By the 10-millisecond mark, droplets achieve a state of equilibrium where their y approximates 0 mm on both the 30° and 45° tilted surfaces. Concerning absolute sliding distances, denoted by x , these are recorded as 0.2 mm for the 30° surface and 0.8 mm for the 45° surface, indicating a shorter droplet displacement on the 30° inclined surface in comparison to the 45° surface. Consequently, this suggests a lower degree of viscous energy dissipation on surfaces with lesser inclination angles.

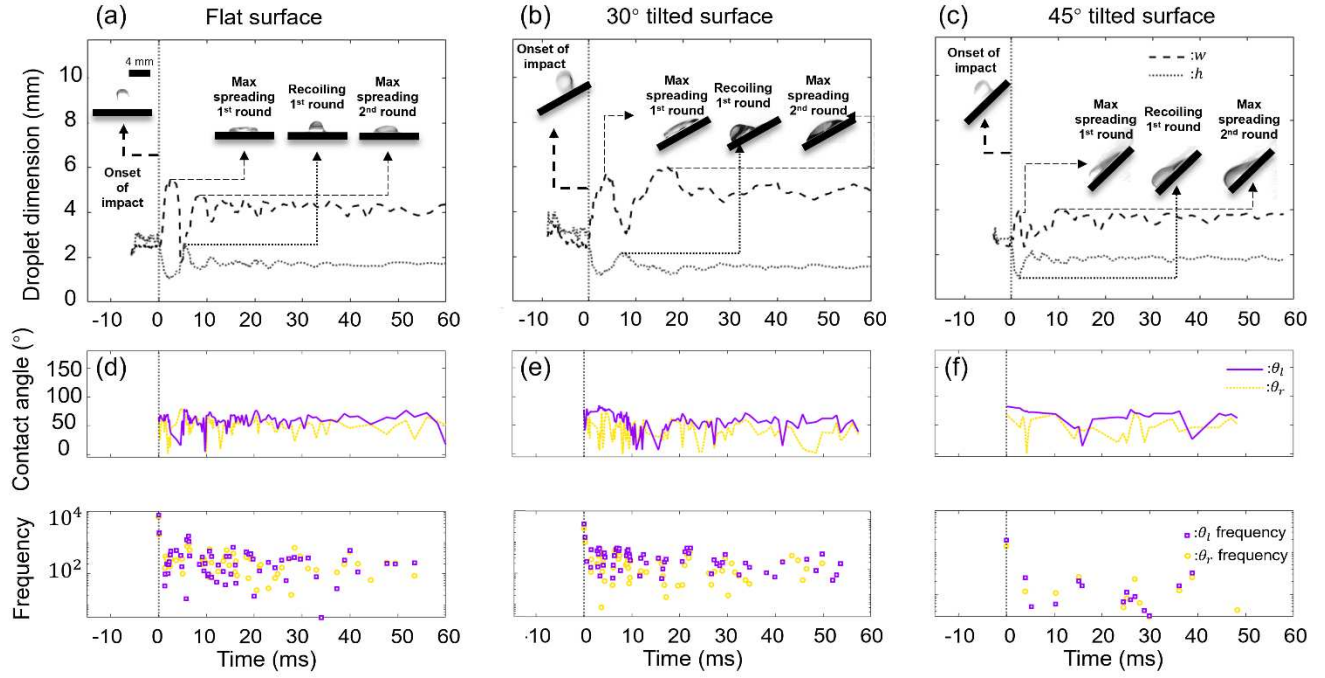


FIGURE 4 Dynamic droplet features such as dimensions and dynamic contact angles. (a) Instantaneous droplet dimensions w (dashed lines) and h (dotted lines) on flat surfaces, (b) on surfaces tilted at 30° , (c) on surfaces tilted at 45° , (d) droplet contact angles θ_l (purple solid lines) and θ_r (yellow dotted lines), and the nFFT frequency of θ_l (purple squares) and θ_r (yellow circles) on flat surfaces, (e) surfaces tilted at 30° , and (f) surfaces tilted at 45° .

The transient nature of droplet impact behavior on both flat and tilted surfaces is characterized by instantaneous droplet dimensions, such as w and h , displayed in **Figures 4a to 4c**. The amplitude peaks for both w and h are more pronounced in **Figures 4a and 4b**, reaching approximately 6 mm for cases of no inclination or smaller inclination angle (30°), while **Figure 4c** exhibits a reduced peak amplitude of around 4 mm on surfaces with larger inclination angle (45°). This distinction highlights the influence of surface orientation on the spreading and vertical displacement of droplets upon impact. Due to the viscous energy dissipation through droplet spreading behavior, we recognize a decaying trend in droplet height h amplitude as time passed in **Figures 4a to 4c**. The amplitudes of droplet width w and height h keep decreasing on flat surface. Contrast to **Figure 4a**, the amplitude of the second peak in w is larger than that of the first peak tilted surfaces in **Figures 4b and 4c**. The spreading motion of the droplet on tilted surfaces is facilitated by the component of gravity acting parallel to the surface, denoted as $mg \cdot \sin \alpha$, which aids in the droplet sliding action and contributes to the increase in the wetted area. The dynamic contact angles refer to interfacial phenomena and are useful information. The magnitude of droplet vibration is quantified through the analysis of time-varying dynamic contact angles (θ_l and θ_r) and their normalized Fast Fourier Transform (nFFT) frequency distribution plots in **Figures 4d to 4f**. These plots are instrumental in defining the intensity of vibrations before the droplets achieve a complete steady state. The concept of a steady state in this context implies the full conversion of droplet kinetic energy into friction-induced heat, internal energy within the droplet, and other forms of energy dissipation. As the component of gravity acting parallel to the surface increases with the surface inclination angle (α), a smaller frequency distribution area is observed on the 45° tilted surface (**Figure 4f**) compared to the flat and 30° tilted surfaces (**Figures 4d and 4e**). This observation suggests that an increased component of parallel-surface gravity accelerates the dissipation of droplet impact energy through viscosity due to a longer sliding distance on the surface, thereby enabling a quicker transition to the steady state.

3.2 Droplet impact forces

In the following section, the features extracted from our framework enable us to compute the impact forces for droplets in both nanoliter and picoliter sizes, in **Figures 5** and **6**, respectively. In addition, we validate the graphically extracted droplet impact force with the impact force model proposed by^{42,43} in SI. For both flat and tilted surfaces, all the droplet impact force $F_{\perp}(\alpha)$ validations are executed at early droplet impact times (i.e., within 0.8 ms upon impact).

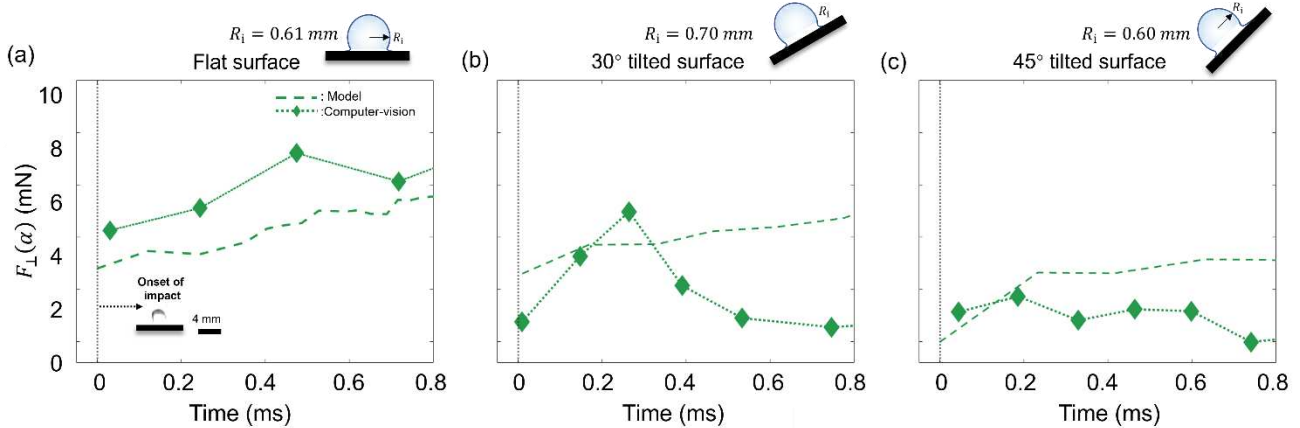


FIGURE 5 Droplet impact force **measurements** for nanoliter droplets. (a) Comparison between time-varying droplet impact force $F_{\perp}(\alpha)$ from the vision-based measurements (green diamonds) and *self-similarity model*⁴² (green dashed lines) on the flat copper surfaces, (b) the comparison on tilted bare copper surfaces with inclination angles of 30°, and (c) the comparison on tilted bare copper surfaces with inclination angles of 45°. Specifically, the initial data points here represent the impact forces calculated from acceleration data obtained from the first three frames right after the impact.

We demonstrate the capability of this vision-based approach to calculate nanoliter droplet impact forces on flat and tilted surfaces. The green dashed lines represent the $F_{\text{model},\perp}$ ^{42,43} as expressed in Eq. (13). For this analysis, droplet initial radii R_i are measured based on the frame showing the onset of droplet impact, which equal 0.61, 0.70, and 0.60 mm for flat, 30°, and 45° tilted surfaces, respectively. While the flat surface shows comparable results of $F_{\perp}(0)$, the deviations between $F_{\perp}(\alpha)$ and $F_{\text{model},\perp}$ in **Figures 5b** to **5c** increase over the time. The *self-similarity* model consistently overestimates $F_{\text{model},\perp}$ compared to calculations derived from the vision-based approach, particularly for cases of 45° tilted surfaces. This discrepancy can be explained with three reasons: (1) The discrepancy arises because droplets on tilted surfaces exhibit both spreading and sliding behaviors⁴¹, in contrast to droplets on flat surfaces, where only spreading phenomenon occurs. It should be noted that the model account for impact behavior only and is only limited to the cases for flat surfaces. The vision-based approach measured sliding distances of droplets on tilted surfaces are 0.19 mm for surfaces with 30° and 0.42 mm for 45° inclination angles, corroborating the earlier statement. The more pronounced overestimation for the 45° tilted surface is due to the greater energy dissipation from frictional forces encountered during the sliding phase, resulting from the increased mobility of the droplet on more steeply angled surfaces. (2) Moreover, the model heavily relies on the droplet dimensions such as w and h . Due to the nature or transient phenomena from bouncing and oscillating behavior, w and h consistently changes, as described in **Figure 4a-4c**, however, this is not well captured. (3) The model solely defines the early stage of droplet impact and is limited to the point of contact so that we report the forces within the time range of 0.8 ms. Note that the calculations are close at the impact point within 0.2 ms for all the cases. This implies that the valid time range corresponding to the *self-similarity* model should be reported within this range.

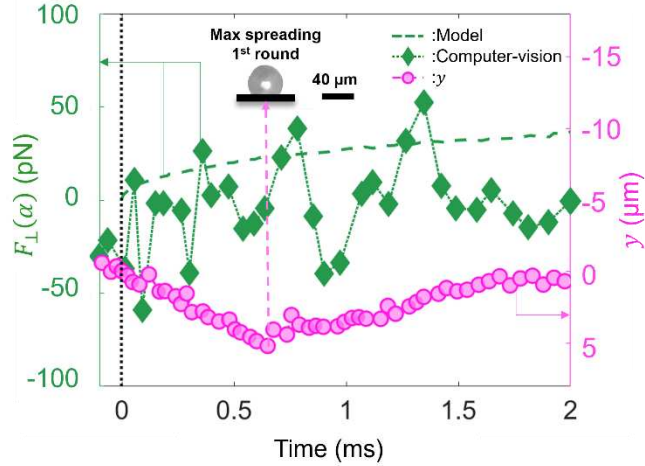


FIGURE 6 Droplet impact force **measurements** for picoliter droplets. Comparison between the time-varying picolitre droplet impact force $F_{\perp}(\alpha)$ within 2 ms upon impact on the flat bare nickel surface obtained from the vision-based approach (green diamonds) and $F_{\perp}(\alpha)$ calculated based on the *self-similarity* model⁴² (green dashed line) at early impact times along with the y on the images (pink circles).

To further test the application of the vision-based approach proposed in this study, we follow the same procedure as utilized above to measure a smaller size of droplet, which is a picolitre droplet. The droplet of a diameter of 44.6 μm and a volume of 46.4 pL is captured at 1,000 fps. **Figure 6** shows the transient droplet impact forces $F_{\perp}(\alpha)$ along with the simultaneous y within 2 ms upon impact. We observe a reasonable agreement between the droplet impact force from the vision-based measurements and the *self-similarity* model⁴² predictions, particularly, near the impact. Here, we notice a similar increase in overestimations from the *self-similarity* model to vision-based approach calculations over time, which reiterates our observation from the previous section. It is also important to highlight that, as depicted in **Figure 6**, our proposed vision-based approach for measuring droplet impact forces achieves a force sensitivity of approximately 10 pN, coupled with a time resolution of hundreds of μs .

4. Conclusion

We propose a fast and efficient machine vision-assisted framework that extracts transient droplet impact data, including droplet velocity, beating frequency, and droplet impact force. This framework processes non-equilibrium droplets and is more versatile, as it can be applied to the conditions where the conventional force sensors are not suitable. Here, the dynamic droplet impact behaviors on non-conventional surfaces, for example, tilted surfaces, are characterized and discussed. The effects of inclination angles on the droplet dimension and beating frequency magnitudes are investigated. In addition, this framework can achieve extreme spatial and temporal resolutions, along with force sensitivity, characterized by measurements in the picoliter range, hundreds of microseconds accuracy, and a force sensitivity of approximately 10 pN, respectively. We verify the feasibility and accuracy of this framework by comparing the droplet impact force results from the vision-based measurements with the *self-similarity* droplet impact force model and with experimental droplet impact force data from previous literature, demonstrating good agreements. In terms of the strength of our proposed vision-based measurement technique, it demonstrates enhanced ability in capturing droplet impact data under a wide array of conditions. Leveraging a novel neuromorphic-based denoising image processing approach, it addresses conditions that have been underexplored by other computer-vision models, such as varying background illumination, textured impact surfaces, and more, showcasing its superior adaptability and precision in complex environments. Providing that the droplet impact conditions are within the camera's field of view and that visually interpretable data is obtainable, our methodology enables a direct analysis of droplet dynamics using the visual information. **To further improve the accuracy of the proposed work, we suggest reconstructing droplet shapes in 3D for centroid computations. This approach may require capturing multiple views instead of relying on a single camera measurement. With the additional enhancement, this technique is poised to make contributions to practical fields, notably in advancing our understanding of water or energy harvesting methods involving droplets, such as raindrops, in future applications.**

5. Methods

5.1 Droplet impact experiments

High-spatial resolution images capturing droplet impact behavior are experimentally attained. The droplet impact processes are explored on both bare copper and nickel substrates, for nanoliter or picolitre droplets, respectively. For the copper substrate⁴¹, we manually polish the 1 cm x 1 cm copper sheets using sandpaper (MacMaster Carr) to make the roughness evenly distributed on the surface. After polishing, we characterize the surface wettability by performing the contact angle measurement with a microscopic contact angle meter (Kyowa Interface Science, MCA-4) from which the contact angle of the copper substrate is 107°. We then test the droplet impact processes on both flat and tilted substrates. We place the copper sheets onto plastic supports with different inclination angles (30° and 45°) to change the inclination angle α of the impacting surface. The fluid for creating the droplets is introduced by a syringe pump (11 Plus, Harvard Apparatus) with 0.3 ± 0.00075 mL/min flow rate. Considering the accuracy limitation of the syringe pump, we place the capillary tip (Kyowa Interface Science) 4.5 cm above the impacting substrates and control the droplet impact velocity at around 1 m/s for all nanoliter droplet cases. Eventually, we collect the sequence of side-view images before and during the droplet impact using a high-speed camera (FASTCAM Mini AX50, Photron; 2,000 frames per second; and 1,024 × 1,024 pixels) on copper substrates. In terms of the picolitre droplet impact experiment, we use the bare nickel with a contact angle of 120° as the flat impact substrates. The microscopic contact angle meter (Kyowa Interface Science, MCA-4) is used to capture the side-view picolitre droplet impact images on nickel substrates with image resolution of 896 × 704 pixels and frame rate at 1,000 – 2,000 frames per second. It contains a precise electric micro-injector system which can generate micro-droplets in a range of 10 to 1,000 pL.

5.2 Neuromorphic-based denoising process

Once we collect the images from a high-speed camera, the images are post-processed to remove the background and noise in the denoising module. To do this, we employ the neuromorphic processing techniques. First, we employ the v2e³⁵ technique (video frames to dynamic-vision-sensor events) to generate denoised event data based on the high-speed optical videos. This process involves automatically transforming the optical video frames into luma frames, where each pixel denotes a brightness value. Following this, the event data are derived by applying brightness intensity-based algorithms on these luma frames. Finally, this data is processed using an event-based image reconstruction tool, implemented as a neural network named FireNet, under the e2vid^{36,37} framework. This step allows us to reconstruct a sequence of droplet impact images, effectively remove video background and noise for clearer visualization.

It is important to note that the reconstruction quality of the final denoised images using the v2e technique is particularly sensitive to two threshold parameters: ‘thres’ and ‘sigma’. Here, ‘thres’ refers to the threshold in logarithmic (log_e) intensity change required to trigger a positive or negative event, while ‘sigma’ represents the one standard deviation threshold variation in logarithmic intensity change. In our practice, ‘thres’ is set at 0.2 and ‘sigma’ at 0.02 to achieve optimal denoised results.

5.3 Data training and extraction

The post-processed images are fed to our customized object detection and object tracking modules, as illustrated in **Figure 2**. The object detection module employs a fast and efficient customized object instance segmentation technique called Mask R-CNN^{34,38}. This neural network is established on the Feature Pyramid Network (FPN) and ResNet101. It allows for automatic segmentation. The model employed in this study is trained on a dataset of 960 images, featuring droplets under condensing on and sliding off a subcooled pipe, with image resolution of 1,280 × 720. In each image, it contains approximately 100 to 200 droplets (96,000 – 192,000 droplets in total), all of which are manually labeled by researchers in Won Lab using Supervisely (a platform helping with the creating, labeling, and annotating the graphical machine-learning training data). Additionally, for validating the accuracy of object detection module, another dataset of 500 to 800 images is annotated. Each image in this dataset displays the side-view of a droplet impacting on flat or tilted surfaces. Details are discussed in **Figures SI1 and SI2 in the Supporting Information**. Next, we harness this trained object detection model to make predictions on a new sequence of droplet impact images. These detected bounding boxes and masks, along with associated object IDs, are then fed into the object tracking module, aiming at extracting the spatiotemporal data of the impacting droplets. We utilize TrackPy in this module, a specialized tracking toolkit^{38–40}, which enables precise monitoring of each droplet's trajectory and movements throughout the image sequence.

5.4 Accuracy validation

The overall performance of the data extraction framework is predominantly controlled by the accuracy of object detecting and tracking modules. We record the accuracy of these two modules by investigating four different scores, including accuracy, recall, F1 score, and precision. The instance detection performance is acceptable based on the evaluation metrics with 99.8% in accuracy, 97.2% in recall, 92.4% in F1-score, and 87.9% in precision. The accuracy of the imaging data extraction is confirmed by using the in-house code that evaluates the scores, as explained in **Figure SI1 in Supporting**

Information.

5.5 Contact angle calculation

Utilizing side-view images of droplets, in this section, we focus on determining the contact angles at two specific liquid-solid contacting points on either side of the droplet. By converting the segmented masks into binary format, we assign a pixel value of 0 to represent the background and a value of 1 to signify the droplet. We employ edge detection tools available in the Matlab Image Processing Toolbox, which are designed to detect significant changes in pixel values (from 1 to 0 or vice versa) within the binary image. This process enables us to delineate a continuous edge profile of the droplet from the binarized segmented masks. Subsequently, we perform curve fitting on the coordinates near the droplet's contact points to derive the curve functions that describe the droplet's profile on both sides as expressed in Eq. (14) and (15).

$$y_l = f_l(x) \quad (14)$$

$$y_r = f_r(x) \quad (15)$$

Finally, we calculate the contact angles from the first derivative of y_l and y_r to determine the contact angles θ_l and θ_r at two contacting points.

$$\theta_l = \text{atan} \frac{dy_l}{dx} \quad (16)$$

$$\theta_r = \text{atan} \frac{dy_r}{dx} \quad (17)$$

References

1. Cook SS. Erosion by water-hammer. *Proc R Soc Lond A Math Phys Eng Sci.* 1928;119(783):481-488.
2. Ahmad M, Schatz MCMV, Casey MV. Experimental investigation of droplet size influence on low pressure steam turbine blade erosion. *Wear.* 2013;303(1-2):83-86.
3. Sharma PP, Gupta SC. Sand detachment by single raindrops of varying kinetic energy and momentum. *Soil Sci Soc Am J.* 1989;53(4):1005-1010.
4. Wang L, Song Y, Xu W, et al. Harvesting energy from high-frequency impinging water droplets by a droplet-based electricity generator. *EcoMat.* 2021;3(4), p.e12116.
5. Kannan R, Vaikuntanathan V, Sivakumar D. Dynamic contact angle beating from drops impacting onto solid surfaces exhibiting anisotropic wetting. *Colloids Surf A Physicochem Eng Asp.* 2011;386(1-3):36-44.
6. Chhasatia VH, Sun Y. Interaction of bi-dispersed particles with contact line in an evaporating colloidal drop. *Soft Matter.* 2011;7(21):10135-10143.
7. Li X, Zhang L, Feng Y, et al. Visualization of Charge Dynamics when Water Droplets Bounce on a Hydrophobic Surface. *ACS nano.* 2023;17(23): 23977-23988.
8. Regtien PPL. Sensors for Mechatronics. Elsevier; 2012.
9. Pruppacher HR, Pitter RL. A semi-empirical determination of the shape of cloud and rain drops. *J Atmos Sci.* 1971;28(1):86-94.
10. Nearing MA, Bradford JM, Holtz RD. Measurement of force vs. time relations for waterdrop impact. *Soil Sci Soc Am J.* 1986;50(6):1532-1536.
11. Li J, Zhang, B, Guo P, Lv Q. Impact force of a low speed water droplet colliding on a solid surface. *J Appl Phys.* 2014;116(21):214903.
12. Zhang B, Li J, Guo P, Lv Q. Experimental studies on the effect of Reynolds and Weber numbers on the impact force of low-speed droplets colliding with a solid surface. *Exp Fluids.* 2017;58(9):1-12.
13. Grinspan AS, Gnanamoorthy R. Impact force of low velocity liquid droplets measured using piezoelectric PVDF film. *Colloids Surf A Physicochem Eng Asp.* 2010;356(1-3):162-168.
14. Mitchell BR, Bate TE, Klewicki JC, Korkolis YP, Kinsey BL. Experimental investigation of droplet impact on metal surfaces in reduced ambient pressure. *Procedia Manuf.* 2017;10:730-736.
15. Haller KK, Ventikos Y, Poulikakos D. Wave structure in the contact line region during high speed droplet impact on a surface: Solution of the Riemann problem for the stiffened gas equation of state. *J Appl Phys.* 2003;93(5):3090-3097.
16. Haller KK, Ventikos Y, Poulikakos D. Computational study of high-speed liquid droplet impact. *J Appl Phys.* 2002;92(5):2821-2828.
17. Chang K-H. Design Theory and Methods using CAD/CAE: The Computer Aided Engineering Design Series. Academic Press; 2014.
18. El-Nasr AA. Evaluation of damping behavior of spray deposited SiC particulates reinforced Al composites. In: Current Advances in Mechanical Design and Production VII. Pergamon; 2000:407-414.
19. Wang H, Jasim A. Piezoelectric energy harvesting from pavement. In: Eco-Efficient Pavement Construction Materials. Woodhead Publishing; 2020:367-382.
20. Troughton MJ. Handbook of Plastics Joining: A Practical Guide. William Andrew; 2008.
21. Delrio FW, Carraro C, Maboudian R. Small-scale surface engineering problems. Tribology and Dynamics of Engine and Powertrain. Woodhead Publishing; 2010:960-989.
22. Chen H, Zhang X, Garcia BD, et al. Drop impact onto a cantilever beam: Behavior of the lamella and force measurement. *Interfacial Phenom Heat Transfer.* 2019;7(1).
23. Viola F. Comparison among different rainfall energy harvesting structures. *Appl Sci.* 2018;8(6):955.
24. Hao G, Dong X, Li Z, Liu X. Water drops impact on a PVDF cantilever: droplet dynamics and voltage output. *J Adhes Sci Technol.* 2021;35(5):485-503.
25. Jellard SCJ, Pu SH, Chen S, Yao K, White NM. Water droplet impact energy harvesting with P(VDF-TrFE) piezoelectric cantilevers on stainless steel substrates. *Smart Mater Struct.* 2019;28(9):095002.
26. Gart S, Mates JE, Megaridis CM, Jung S. Droplet impacting a cantilever: A leaf-raindrop system. *Phys Rev Applied.* 2015;3(4):044019.
27. Dong X, Huang X, Liu J. Modeling and simulation of droplet impact on elastic beams based on SPH. *Eur J Mech A Solids.* 2019;75:237-257.
28. Canny J. A Computational Approach to Edge Detection. *IEEE Trans Pattern Anal Mach Intell.* 1986;PAMI-8(6):679-698.
29. Lim JS. Two-Dimensional Signal and Image Processing. Prentice-Hall, Inc; 1990:478-488.

30. Chow CK, Kaneko T. Boundary detection of radiographic images by a threshold method. In: *Frontiers of Pattern Recognition*. Academic Press; 1972:61-82.
31. Espindola GM, Camara G, Reis IA, Bins LS, Monteiro AM. Parameter selection for region-growing image segmentation algorithms using spatial autocorrelation. *Int J Remote Sens*. 2006;27(14):3035-3040.
32. Li N, Huo H, Zhao YM, Chen X, Fang T. A spatial clustering method with edge weighting for image segmentation. *IEEE Geosci Remote Sens Lett*. 2013;10(5):1124-1128.
33. Visin F, Ciccone M, Romero A, Kastner K, Cho K, Bengio Y, Matteucci M, Courville A. Reseg: A recurrent neural network-based model for semantic segmentation. In: *Proceedings of the IEEE conference on computer vision and pattern recognition workshops*. 2016;pp.41-48.
34. He K, Gkioxari G, Dollar P, Girshick R. Mask r-cnn. *Proceedings of the IEEE International Conference on Computer Vision*. 2017.
35. Delbruck T, Hu Y, He Z. V2E: From video frames to realistic DVS event camera streams. *arXiv preprint arXiv:2006*. <https://arxiv.org/abs/2006> (Submitted June 13, 2020. Accessed March 1, 2022.).
36. Cadena PRG, Qian Y, Wang C, Yang M. SPADE-E2VID: Spatially-Adaptive Denormalization for Event-Based Video Reconstruction. *IEEE Trans Image Process*. 2021;30:2488-2500.
37. Scheerlinck C, Rebecq H, Gehrig D, Barnes N, Mahony R, Scaramuzza D. Fast image reconstruction with an event camera. *Proc IEEE/CVF Winter Conf Appl Comput Vis*. 2020.
38. Suh Y, Lee J, Simadiris P, Yan X, Sett S, Li L, Rabbi KF, Miljkovic N, Won Y. A Deep Learning Perspective on Dropwise Condensation. *Adv Sci*. 2021;8(22):2101794.
39. Suh Y, Bostanabad R, Won Y. Deep learning predicts boiling heat transfer. *Sci Rep*. 2021;11(1):1-10.
40. Suh Y, Chang S, Simadiris P, Inouyet T, Hoque MJ, Khodakarami S, Kharangate C, Miljkovic N, Won Y. VISION-iT: Deep Nuclei Tracking Framework for Digitalizing Bubbles and Droplets. 2023; Available at SSRN 4491956.
41. Zhao C, Montazeri K, Shao B, Won Y. Mapping between surface wettability, droplets, and their impacting behaviors. *Langmuir*. 2021;37(33):9964-9972.
42. Philippi J, Lagrée PY, Antkowiak A. Drop impact on a solid surface: short-time self-similarity. *J Fluid Mech*. 2016;795:96-135.
43. Zhang R, Zhang B, Lv Q, Li J, Guo P. Effects of droplet shape on impact force of low-speed droplets colliding with solid surface. *Exp Fluids*. 2019;60(4):1-13.
44. Jayawardena AW, Rezaur RB. Measuring drop size distribution and kinetic energy of rainfall using a force transducer. *Hydrol Process*. 2000;14(1):37-49.
45. Mitchell BR, Klewicki JC, Korkolis, YP, Kinsey BL. The transient force profile of low-speed droplet impact: measurements and model. *J. Fluid Mech*. 2019;867, pp.300-322.
46. Lichtensteiner P, Posch C, Delbruck T. A 128x128 120dB 15 μ s Latency Asynchronous Temporal Contrast Vision Sensor. *IEEE Journal of Solid-State Circuits*. 2008;(2):566-76.
47. Nozaki Y, Delbruck T. Temperature and parasitic photocurrent effects in dynamic vision sensors. *IEEE Trans Electron Devices*. 2017;64(8):3239-3245.

Acknowledgements

C.Z. expresses gratitude for the financial assistance received from the UCI Mechanical and Aerospace Engineering Department through the Graduate Dean's Dissertation Fellowship. Special acknowledgment goes to Quang Pham and Bowen Shao for their contribution of experimental droplet impact data, as well as to undergraduate students in Won Lab for their efforts in annotating droplets in images. The authors acknowledge the support from National Science Foundation (award number 2045322).

Conflict of Interest

The authors declare no conflict of interest.

Additional Information

Additional supporting information can be found online in the Supporting Information section at the end of this article.

Nomenclatures

a	acceleration (m^2/s)
f	droplet edge curve function
g	gravitational acceleration (m^2/s)
h	droplet height (mm)
m	droplet weight (g)
t	droplet impact time (s)
u	droplet impact velocity in the x-direction (m/s)
v	droplet impact velocity in the y-direction (m/s)
w	droplet width (mm)
x	x coordinates of the droplet centroid (mm)
y	y coordinates of the droplet centroid (mm)
A	side-view area of droplet (mm^2)
D	droplet diameter (mm)
F	force (N)
R	droplet radius (m)
V	droplet volume (m^3)
α	inclination angle of the impacting surface ($^\circ$)
θ	dynamic contact angle ($^\circ$)
ρ	water droplet density (kg/m^3)

Subscripts

0	average droplet velocity within 2 ms before the onset of impact
e	effective diameter of droplets
i	at the onset of impact
l	left
model	total droplet impact force calculated by <i>self-similarity</i> model
r	right
x	direction normal to the gravity force
y	direction parallel to the gravity force
N	supporting force from impacting surface
μ	frictional force from impacting surface
\perp	direction normal to the impacting surface (perpendicular-surface direction)
\parallel	direction parallel to the impacting surface (parallel-surface direction)